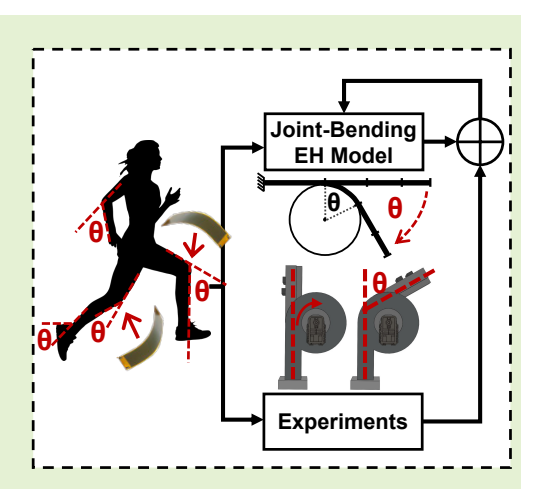
# Wearable Piezoelectric Energy Harvesting from Human Gait: Modeling and Experimental Validation

Yigit Tuncel, Toygun Basaklar, and Umit Ogras

Abstract—Wearable devices with a flexible and stretchable form factor enable novel and attractive applications. The promising outlook for these devices is hindered by their limited battery capacity constrained by size and other physical limitations. Motion energy harvesting can alleviate these challenges and reduce dependency on batteries. Despite this potential, a definitive capacity for wearable motion energy harvesting has yet to be identified. To facilitate the exploration of this capacity, we propose an analytical model for the energy harvesting potential of a wearable piezoelectric energy harvester placed on the knee joint. In addition, we validate the proposed model extensively with a prototype piezoelectric energy harvester. Our results show that the proposed model estimates the harvested power with less than 5% mean absolute percentage error for all gait speeds and various transducer configurations. In addition, the proposed harvester can generate 161  $\mu$ W power at 5 mph. We further show that this amount can sustain a 35  $\mu$ A load.

Index Terms— Analytical modeling, edge computing, energy harvesting, loT, piezoelectric, wearable device.



## I. INTRODUCTION

State-of-the-art wearable sensing and computing technology enable remote monitoring and data analytics for users in home environments. This technology has exciting and crucial applications such as telepathic diagnostics, biofeedback, activity-tracking, and preventive medicine [2]–[10]. However, recent user surveys and studies reveal that the frequent charging and maintenance requirements hinder their widespread adoption [2], [11]. The root cause of this limitation is small battery capacities, which stem from the small form factor and low-cost constraints of wearable devices. For example, the Oura Ring 3 incorporates a 22 mAh – 3.7 V battery and advertises a battery life of 4 to 7 days [12], [13]. Using energy harvesting (EH) as an orthogonal energy source can alleviate these limitations by decreasing battery dependency.

Wearable EH modalities generate electrical energy from various sources in a user's environment while conforming to the physical and comfort constraints associated with the wearable form factor [14]. The most common energy sources are light, motion, electromagnetic waves, and heat [15]. Ambient light has the highest potential for wearable EH devices. For instance, with an 8.1-cm<sup>2</sup> flexible PV-cell, ambient light

This work was supported in part by DARPA Young Faculty Award (YFA) Grant D14AP00068 and NSF CAREER award CNS-1651624

Yigit Tuncel, Toygun Basaklar and Umit Ogras are with the Department of Electrical and Computer Engineering, University of Wisconsin-Madison, Madison, WI 53706 USA (e-mail: {tuncel, basaklar, uo-gras}@wisc.edu)

An earlier version of this paper was presented at the 2020 ACM/IEEE International Symposium on Low Power Electronics and Design (ISLPED) [1] and was published in its proceedings (doi: https://doi.org/10.1145/3370748.3406578).

EH offers a capacity of over 1 mW outdoors (5000 lux) and close to 100  $\mu W$  indoors (5000 lux) [16]. Similarly, radiofrequency (RF) EH can harvest 10  $\mu W$  with an 18.4-cm² flexible antenna with a signal strength of -10 dBm at 915 MHz [17]. Body-heat EH has power levels of about 3  $\mu W$  with a 1-cm² flexible harvester at an ambient temperature of 15°C (i.e., a temperature difference of 22°C) [18]. Humanmotion EH is particularly interesting for wearable applications because the energy is available on demand. In addition, it can harvest about 15  $\mu W$  with a 23.8-cm² piezoelectric transducer while the wearer is walking [1], [19]. Therefore, motion energy is an attractive energy source for wearable EH devices.

Researchers have developed numerous designs for wearable motion EH devices to capture and transduce kinetic energy from parts of the body, such as the foot [20], [21], knee joint [1], [22], [23], and arm [24]. These designs employ electromagnetic, triboelectric, or piezoelectric energy transduction. Electromagnetic harvesters are bulky due to their magnets, coils, and other common components [22]. Triboelectric harvesters have not yet achieved sufficiently high power levels, are limited to research, and are expensive to manufacture [25]. In contrast, piezoelectricity-based energy harvesters (PEHs) offer practical power levels ( $\mu$ W-mW) with a relatively small and flexible form factor at an affordable material cost.

The physical flexibility of PEHs relies on novel materials such as polyvinylidene fluoride (PVDF) and macro-fiber composite (MFC). Designs that incorporate these materials can be placed directly on human joints [26]. Very few studies investigated the potential of a wearable PEH modality despite its promising outlook [26], [27]. As a result, a definitive exploration of this capacity is still absent from the literature.

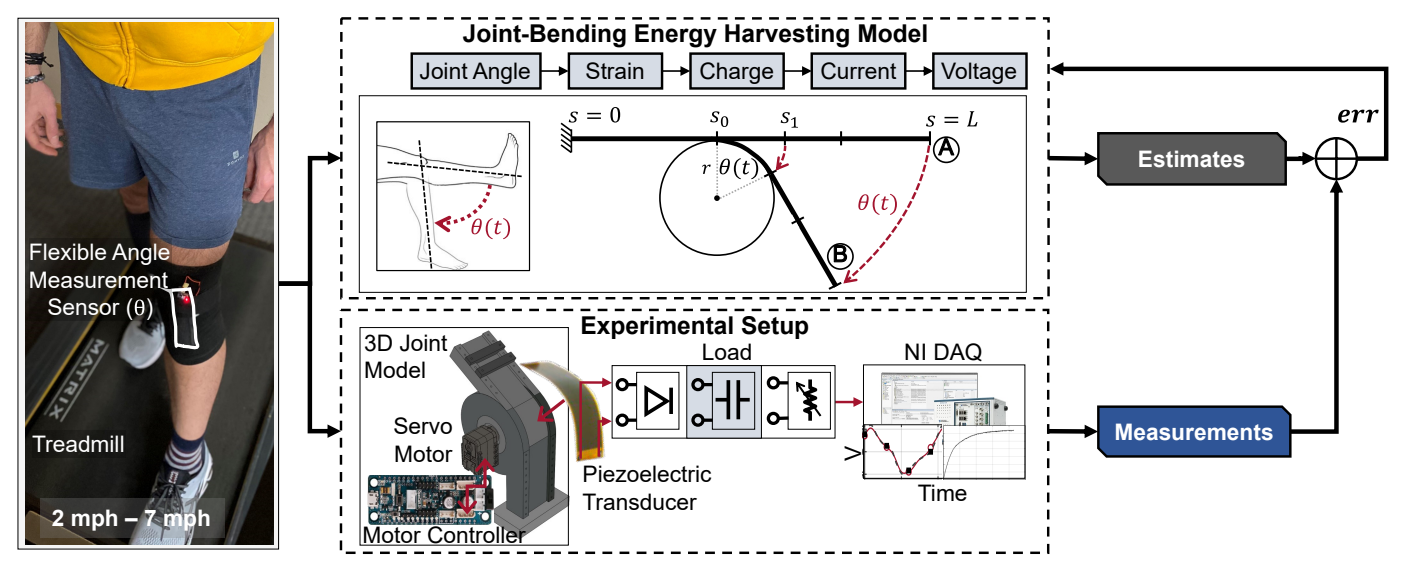


Fig. 1: Overview of the modeling steps and experimental procedure.

A quantitative analysis of this topic would benefit hardware designers, system-level designers, and application developers. Furthermore, prior studies follow a purely experimental approach and *do not model the EH mechanism*. A model-based approach is critical for identifying dependencies to parameters in a given system and predicting harvested energy in real-life scenarios. These predictions are needed to enable smart energy management techniques to achieve energy-neutral operation [28], [29]. Therefore, there is also a strong need for modeling PEH directly from joint bending.

To address the gaps in the literature, this study investigates the EH potential of MFC transducers placed on the knee during human gait, as shown in Figure 1. We focus on the knee joint due to three primary reasons: (1) The biomechanical energy potential at the knees is higher than other joints [30], (2) knees follow a periodic trajectory, which allows for continuous harvesting of energy while the person wearing the device is walking, and (3) knee joint monitoring opens up a variety of possible applications, ranging from walking aid for patients to fatigue detection in athletes [31], [32]. To this end, we first present a novel and comprehensive analytical model for the EH output of a piezoelectric transducer directly placed on a joint. Then, we present an extensive experimental exploration that validates the proposed model. Our experimental results also demonstrate the EH potential of wearable knee joint-bending PEH for various gait speeds, including walking, jogging, and running. Our prototype PEH harvests 46 µW power from the knee joint while the user is walking and 161 µW while the user is jogging. These results are significantly higher than the EH capacity of other wearable PEHs in the literature [26], [27], [33], [34]. Hence, this study demonstrates the viability of a PEH device worn at the knee joint for low-power applications. For example, the produced power can sustain a variety of low-power wearable applications, ranging from human activity recognition [35] to cardiac arrythmia detection [36].

In summary, this paper makes three major contributions:

- A closed-form expression for flexible joint-bending piezoelectric EH with less than 5% modeling error.
- A novel PEH prototype in the form of a knee sleeve

- capable of harvesting energy from the joint-bending movements of the knee during human gait.
- Experimental results that show up to 161  $\mu$ W generation and 35- $\mu$ A sustained constant current load at 1.8V at a 5 mph gait speed.

The rest of the paper is organized as follows. We review the related work in Section II. Next, we present the analytical model for the capacity of joint-bending EH in Section III. Section IV explains our experimental procedure and presents a thorough analysis of our experimental findings. In Section V, we provide detailed information and valuable insights about the experimental setup and the operation principles of the energy harvester. Section VI concludes the paper.

# II. RELATED WORK

The frequency of human motion is in the order of a few Hertz, which is at least an order of magnitude smaller than the resonant frequency of piezoelectric transducers. In the wearable PEH literature, researchers have proposed numerous frequency up-conversion schemes and techniques for the vibration of piezoelectric material at the resonant frequency to obtain maximum power [23], [37]-[39]. However, these techniques often result in bulky and inflexible devices, uncomfortable to wear. For example, a recent study [37] uses 16 PZT-5H (483 mm<sup>2</sup>) piezoelectric transducers placed in a circular frame mounted on the leg. It also uses 40 cube magnets (27 mm<sup>3</sup>) in total to up-convert the walking frequency. Although the generated power is close to 6 mW, the design is bulky and lacks a flexible form factor, rendering the device impractical for wearable applications. In contrast, we utilize the flexibility of the MFC and use the large-bending movement of the knee as the energy source.

Few studies have investigated the EH potential stemming from the direct placement of piezoelectric materials on the joints. Proto et al. [26] place two different types of piezoelectric transducers, LDT4-028k (2964 mm<sup>2</sup>) and P-876.A12 (1500 mm<sup>2</sup>), at various locations on the body and record the harvested energy during walking, jogging, and running.

TABLE I: Compilation of recent related studies on wearable PEHs

Ref	Analytical Model	Experimental Validation	Large Bending	Flexible Form factor	Size	Source	Reported Power
[37]	✓	<b>✓</b>	Х	Х	$\sim$ 308 cm <sup>3</sup> *	Walk	6 mW
[33]	✓	×	X	✓	$1476 \text{ mm}^2$	Walk	1.0 μW
[34]	✓	×	X	✓	$3000 \text{ mm}^2$	Walk/Run	6.2/12 μW
[26]	X	✓	✓	✓	$2964 \text{ mm}^2$	Walk/Jog	1.9/3.7 μW
[27]	X	✓	✓	✓	$2380 \text{ mm}^2$	1.5 Hz	0.9 μW
Our Study	✓	✓	✓	✓	$2380 \text{ mm}^2$	2-7 mph	<b>46</b> – <b>161</b> μW

<sup>\* [37]</sup> does not specifically disclose the size. We deduced it from the 88-mm inner diameter and the 12.7-mm height.

According to their results, P-876.A12 harvests 2.21 µW from walking, 5.98 μW from jogging, and 23.70 μW from running. Similarly, LDT4-028k harvests 1.90 µW, 3.71 µW, and 8.83 μW from walking, jogging, and running, respectively. Another study uses a mechanical frame to explore the dynamics of EH from human gait [27]. The authors place an MFC8528P2 (2380 mm<sup>2</sup>) piezoelectric transducer on the frame and observe close to 1 µW generated power from walking motion. Another similar study places two P-876.A12 (1500 mm<sup>2</sup>) piezoelectric transducers on the front and back of the knee. Their results suggest that the transducers harvest more power on the front of the knee than on the back. Specifically, they report a total harvested power of 6.2 µW from walking and 12 µW from running [34]. These studies – despite their helpful insights into the potential for wearable PEHs – are purely experimental and lack the analytical modeling of the EH mechanism at the heart of these PEHs. Moreover, the generated power is significantly lower than our results.

Analytical modeling is critical as it sheds light on dependencies on various parameters in a system. It also enables realistic energy estimates from a wide array of motions. Although the piezoelectric EH has been extensively modeled in the literature [40], [41], the added flexibility and large-bending conditions in a wearable ecosystem can render the previous modeling approaches obsolete. For example, the authors in [42] show that the models for traditional rigid PV-cells give poor accuracy for flexible PV-cells. Similarly, [33] is the first study in the literature that provides a theoretical analysis of the power generated from a flexible PVDF transducer placed on the human knee. Throughout the analysis, the author uses a small-angle approximation for the bending of the piezoelectric transducer. This approach is inadequate, as human joint motions involve movements that execute large-bending angles. Moreover, the authors do not validate the proposed model through experimental measurements. Our previous work [1] provides a mathematical model for the power harvested from

the large-bending joint movements. Its main result is a differential equation that governs the voltage at the terminals of the piezoelectric transducer. This mathematical model is validated only under ideal sinusoidal actuation. In contrast, our present study extends the main theoretical result of our previous study to a closed-form solution for PEH based on low-frequency, large-bending joint movements. Furthermore, we validate the model with realistic actuation recorded from the knee at several gait speeds using a robotic 3D-printed human knee. Thus, the current study explores the capacity of a flexible knee joint PEH under real use-cases and proposes a modeling framework for analyzing the EH capacity of other movements and joints.

## III. JOINT-BENDING ENERGY HARVESTING MODEL

This section describes the proposed analytical model for EH from large-bending joint movements. Section III-A introduces key considerations for our proposed large-bending joint model and highlights the differential equation that governs the voltage generated by the piezoelectric transducer from our previous study [1]. Then, Section III-B extends the differential equation to a closed-form solution for the RMS voltage and power generated by a flexible PEH with a step-by-step derivation.

## A. Joint Bending PEH Model Overview

We consider a flexible piezoelectric transducer placed directly on a joint, as shown in Figure 2. The mechanical forces due to joint bending acting on the piezoelectric material are much larger than the electrical forces induced by the piezoelectric material. This observation allows us to decouple the mechanical and electrical domains and analyze them separately. First, in the mechanical domain, the physical displacement is modeled under *large-bending conditions*, which captures angles larger than 10°. We use this physical displacement to obtain the strain induced on the piezoelectric transducer. Then,

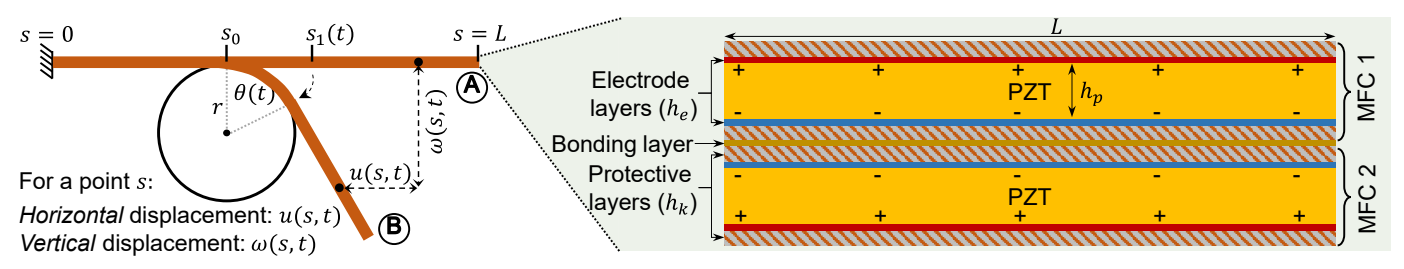


Fig. 2: Left: Large joint bending representation using a cantilever beam over a circular support. Right: The bimorph piezoelectric transducer used in this work.

in the electrical domain, the strain is converted to the generated current (and voltage) between the terminals of the piezoelectric transducer.

**Mechanical Domain:** To formulate the displacement, we use the large-bending representation of a cantilever beam over a circular support, as shown in Figure 2. The joint is modeled as circular support with radius r, while the piezoelectric transducer is a beam that bends along the circular support according to joint bend angle  $\theta$ . The neutral position of the transducer is shown with the flat line (A). As the joint bends, the transducer moves from position (A) to (B), taking a curved form. In this illustration, positions s=0 and s=Lshow the transducer's clamped (i.e., fixed) and free ends, respectively. The point marked by  $s = s_0$  is the first point that touches the circle, while  $s = s_1$  is the last point that touches the circle. Using the arc length on the circular profile, we obtain  $s_1(t)=s_0+r\theta(t)$ , where  $\theta(t)$  is the bending angle. Then, using  $s_1(t)$ , the proposed model expresses the horizontal displacement u(s,t) of an arbitrary point s for  $0 \le s \le L$  as:

$$u(s,t) = \begin{cases} 0, & 0 \le s \le s_0 \\ s_0 + r\sin\left(\frac{s-s_0}{r}\right) - s, & s_0 \le s \le s_1(t) \\ s_0 + r\sin\theta(t) + \\ (s - s_1(t))\cos\theta(t) - s, & s_1(t) \le s \le L \end{cases}$$
(1)

The strain on the piezoelectric transducer is a function of its curvature. From the geometry of the problem, the curvature of the piezoelectric transducer is equal to the curvature of the circular support:

$$\kappa(s,t) = \begin{cases} \frac{1}{r}, & s_0 \le s \le s_1(t) \\ 0, & otherwise \end{cases}$$
(2)

Then, the average strain in the piezoelectric transducer from the large-bending representation is calculated as a function of horizontal displacement and curvature [43] as follows:

$$S_1(s,t) = -h_{pc}\kappa(s,t) + \frac{\partial u(s,t)}{\partial s}$$
 (3)

where  $h_{pc}=h_k+h_e+rac{h_p}{2}$  is the distance to the neutral axis in the thickness direction of the piezoelectric transducer [40]. The piezoelectric transducers we use (MFC8528P2) can be modeled as composite beams with five layers, as shown in Figure 2. They consist of a flexible substrate/protective layer at the outsides, electrode layers after that ((-)negative on one side, (+)negative on the other), and a piezoelectric layer between them. When two of these transducers are bonded together, the neutral axis falls precisely on the interface, and the amplitudes of the average strain on the piezoelectric layers on the two sides are equal. With this formulation, we ignore other acting forces on the piezoelectric transducer, such as the friction force. To satisfy this assumption, we design the experimental setup to exert minimal extra forces on the transducer, as explained in Section IV. Next, we use the average strain to obtain the generated electrical power by the piezoelectric transducer.

**Electrical Domain:** To formulate the generated power, we first obtain the accumulated charge in the piezoelectric material

by applying the Gauss Law to the electric displacement field inside the material along the thickness axis:

$$Q(t) = \int_0^W \int_0^L \left( \epsilon_{33}^S E_3^S(t) + Y_p d_{31} S_1(s, t) \right) dW ds \qquad (4)$$

where  $\epsilon_{33}^S$  is the permittivity under constant strain,  $d_{31}$  is the electromechanical coupling coefficient,  $Y_p$  is the Young's Modulus of the piezoelectric layer,  $E_3^S(t)$  is the electric field within the piezoelectric layer, and W and L denote the width and length of the piezoelectric patch, respectively. Since  $E_3^S$  is constant along the area and  $S_1$  is constant along the width of the patch, the integrals simplify to:

$$Q(t) = \epsilon_{33}^{S} W L E_3^{S}(t) + Y_p d_{31} W \int_0^L S_1(s, t) ds$$
 (5)

 $E_3^S(t)$  is equal to the voltage divided by the thickness of the piezoelectric layer:  $E_3^S(t)$ = $-\frac{V(t)}{h_p}$ . Substituting the electric field and strain expressions, the electric charge is found as:

$$Q(t) = -\frac{\epsilon_{33}^S WL}{h_p} V(t) + Y_p d_{31} W \int_0^L \left( -h_{pc} \kappa(s,t) + \frac{\partial u(s,t)}{\partial s} \right) ds \tag{6}$$

In Equation 6, the term  $\frac{\epsilon_{33}^S WL}{h_p}$  is referred to as the capacitance of the patch [40], and is denoted by C from here on. To evaluate the integral in Equation 6, we consider the two terms inside the integral separately. Since  $\kappa(s,t)=0$  for  $s< s_0$  and  $s>s_1(t)$ , the first term evaluates to:

$$\int_{0}^{L} -h_{pc}\kappa(s,t)ds = \int_{s_{0}}^{s_{1}(t)} -h_{pc}\kappa(s,t)ds = \int_{s_{0}}^{s_{0}+r\theta(t)} -h_{pc}\frac{1}{r}ds$$

$$= -h_{pc}\theta(t)$$
(7)

For the second term in Equation 6, since u(s,t) is continuous at  $s=s_0$  and  $s=s_1(t)$ , we can integrate it as:

$$\int_{0}^{L} \frac{\partial u(s,t)}{\partial s} ds = u(L,t) - u(0,t)$$

$$= u(L,t)$$
(8)

With these, Equation 6 reduces to:

$$Q(t) = -CV(t) + Y_n d_{31}W \left(-h_{nc}\theta(t) + u(L, t)\right)$$
 (9)

Next, we take the time derivative of Q(t) to obtain the electrical current generated by the piezoelectric patch:

$$\frac{dQ(t)}{dt} = -C\frac{dV(t)}{dt} + Y_p d_{31}W \left(-h_{pc}\frac{d\theta(t)}{dt} + \frac{\partial u(L,t)}{\partial t}\right) \quad (10)$$

We obtain  $\frac{\partial u(L,t)}{\partial t}=(s_1(t)-L)\frac{d\theta(t)}{dt}sin\theta(t)$  from Equation 1. Then, from  $V(t)=\frac{dQ(t)}{dt}R_L$ , we obtain the differential equation that governs the voltage generated by the piezoelectric transducer as follows:

$$\frac{dV(t)}{dt} = \frac{-V(t)}{R_L C} - \frac{Y_p d_{31} W}{C} \left[ h_{pc} \frac{d\theta(t)}{dt} - (s_1(t) - L) \frac{d\theta(t)}{dt} sin\theta(t) \right]$$
(11)

where  $R_L$  is the load connected to the piezoelectric transducer. The parameters and variables used in these equations are summarized in Table II.

TABLE II: Table of notation.

Symbol	Parameter	Symbol	Parameter
$\overline{V}$	Generated voltage	$\overline{Q}$	Accumulated charge
$S_1$	Axial strain	$\stackrel{Y_p}{L}$	PZ Young's modulus
$\omega$	Vert. displacement	$\hat{L}$	PZ length
u	Horz. displacement	W	PZ width
$\kappa$	Curvature	C	PZ capacitance
$\theta$	Joint bending angle	$R_L$	PZ load
r	Radius of curvature	$h_p^-$	PZ thickness
$E_3^S$	Electric field	ı.	Protective layer
$E_3$	within PZ	$h_k$	thickness
$\epsilon^S_{33}$	Permittivity under	1.	Electrode layer
	constant strain	$h_e$	thickness
J	Electromechanical	L	Distance to
$d_{31}$	coupling coeff. [43]	$h_{pc}$	neutral axis

PZ: Piezoelectric Transducer

## B. Analytical Closed-form Solution

Equation 11 is an ordinary differential equation. There are three main benefits of finding an analytical closed-form solution over the differential equation:

- 1) Analytical solutions are better than differential equations at providing useful insights into both the dependency on parameters and the relative importance of the parameters,
- 2) They are more reliable than differential equations since they do not suffer from numerical instabilities,
- 3) They require significantly lower computational effort for parameter sweeps and fitting than numerical approaches.

In addition, in the EH context, an analytical solution for the power output of the system can be used to develop novel maximum power point tracking algorithms. Thus, this section provides the derivation of an analytical closed-form solution for the RMS power generated by the piezoelectric transducer.

We solve Equation 11 to obtain the expression for V(t) as:

$$V(t) = \frac{Y_p d_{31} W}{C} e^{\frac{-t}{RC}} \int_{\tau=0}^{t} \left( -h_{pc} \frac{d\theta(t)}{dt} + \sin\theta(t) \left( s_1(t) - L \right) \frac{d\theta(t)}{dt} \right) d\tau$$
(12)

A closed-form solution for the integral in Equation 12 does not exist. To overcome this obstacle, we assume that the motion is periodic (i.e.,  $\theta$  is a periodic waveform). We validate this assumption in Section IV by illustrating knee angle recordings at different gait speeds. Then, we use the Fourier series expansion of  $\theta(t)$ :

$$s_{\theta}(t) = a_0 + \sum_{k=1}^{K} [a_k coskt + b_k sinkt]$$

It follows that  $\frac{ds_{\theta}(t)}{dt} = \sum_{k=1}^{K} [b_k coskt - a_k sinkt]$ . Similarly, we use the Fourier series expansion of the second term in the integral  $g(t) = sin\theta(t) \left(s_1(t) - L\right) \frac{d\theta(t)}{dt}$  in Equation 12:

$$s_g(t) = a_0^* + \sum_{m=1}^{M} [a_m cosmt + b_m sinmt]$$

Here, K and M denote the number of Fourier components. Next, we plug these Fourier series expansions of the two components into the integral in Equation 12 and evaluate the

TABLE III: Coefficients used in Equation 13 and onwards.

$$\begin{array}{ll} \hline \alpha_k = a_k C k^2 + \frac{b_k k}{R_L} & \alpha_m = \frac{a_m}{R_L} - b_m C m \\ \beta_k = b_k C k^2 - \frac{a_k k}{R_L} & \beta_m = \frac{b_m}{R_L} - a_m C m \\ \gamma_k = -a_k C k^2 - \frac{b_k k}{R_L} & \gamma_m = -\frac{a_m}{R_L} + b_m C m \end{array}$$

integral. After some algebra and simplifications, we obtain the following expression:

$$V(t) = Y_{p}d_{31}W \left[ -h_{pc} \sum_{k=1}^{K} \frac{\alpha_{k}coskt + \beta_{k}sinkt + \gamma_{k}e^{\frac{-t}{R_{L}C}}}{\frac{1}{R_{L}^{2}} + C^{2}k^{2}} + (-a_{0}^{*}R_{L})(e^{\frac{-t}{R_{L}C}} - 1) + \sum_{m=1}^{M} \frac{\alpha_{m}cosmt + \beta_{m}sinmt + \gamma_{m}e^{\frac{-t}{R_{L}C}}}{\frac{1}{R_{L}^{2}} + C^{2}m^{2}} \right]$$
(13)

where  $\alpha_k$ ,  $\beta_k$ ,  $\gamma_k$ ,  $\alpha_m$ ,  $\beta_m$ , and  $\gamma_m$  are given in Table III.

We can further simplify Equation 13 by eliminating the transient terms (i.e., by taking the limit  $\lim_{t\to\infty}V(t)$ ) and obtain the steady-state voltage  $V_{ss}(t)$  as:

$$V_{ss}(t) = Y_p d_{31} W \left[ a_0^* R_L - h_{pc} \sum_{k=1}^K \frac{\alpha_k coskt + \beta_k sinkt}{\frac{1}{R_L^2} + C^2 k^2} + \sum_{m=1}^M \frac{\alpha_m cosmt + \beta_m sinmt}{\frac{1}{R_L^2} + C^2 m^2} \right]$$
(14)

Equation 14 is a sum of sinusoids with a DC offset in the following form:  $f(t) = F_0 + F_1 cos(\omega_1 t + \Theta_1) + ... + F_n cos(\omega_n t + \Theta_n)$ . The RMS value of such a function is given by:  $F_{RMS} = \sqrt{F_0^2 + \frac{F_1^2}{2} + ... + \frac{F_n^2}{2}}$ . Using this expression with Equation 14, we calculate the RMS voltage  $V_{RMS}$  generated by the piezoelectric transducer, as follows:

$$V_{RMS} = Y_p d_{31} W \sqrt{a_0^{*2} R_L^2 + \frac{h_{pc}^2}{2} \sum_{k=1}^K \frac{\alpha_k^2 + \beta_k^2}{\left(\frac{1}{R_L^2} + C^2 k^2\right)^2}} + \frac{1}{2} \sum_{m=1}^M \frac{\alpha_m^2 + \beta_m^2}{\left(\frac{1}{R_L^2} + C^2 m^2\right)^2}$$
(15)

Finding the Generated Power: Finally, RMS power harvested by the transducer is given by  $P_{RMS} = \frac{V_{RMS}^2}{R_T}$ :

$$P_{RMS} = \frac{(Y_p d_{31} W)^2}{R_L} \left( a_0^{*2} R_L^2 + \frac{h_{pc}^2}{2} \sum_{k=1}^K \frac{\alpha_k^2 + \beta_k^2}{\left(\frac{1}{R_L^2} + C^2 k^2\right)^2} + \frac{1}{2} \sum_{m=1}^M \frac{\alpha_m^2 + \beta_m^2}{\left(\frac{1}{R_L^2} + C^2 m^2\right)^2} \right) f$$
(16)

where f is a fitting parameter to adjust the model response to experimental measurements. We justify the need for it for three main reasons: (1) The neglected change in the parameter

 $h_{pc}$  due to the epoxy layer for bonding, (2) a possible slight misalignment between the two transducers, and (3) the additive uncertainty in the capacitance of each piezoelectric transducer. The value for f is found for a given transducer with the help of experimental measurements. In the present study, we calculate it such that the normalized mean squared error between the experiments and model outputs are minimized:

Find f such that 
$$\min_{f} \sum_{R_L} \frac{||P_{ref} - \hat{P}_{RMS}(f)||^2}{||P_{ref} - \frac{1}{N} \sum_{n=1}^{N} P_{ref}||^2}$$
 (17)

where  $P_{ref}$  is the experimental RMS power,  $\hat{P}_{RMS}$  is the model RMS power output given by Equation 16 and N is the number of samples in the experimental recording.

## IV. EXPERIMENTAL EVALUATION OF JOINT BENDING EH

This section first introduces the experimental setup and procedure used in our evaluations. Then, we present the generated power by the flexible piezoelectric transducers. Finally, we provide energy measurements at the input and output (load) sides of the energy harvester.

## A. Experimental Setup and Procedure

Obtaining reproducible results is critical in a validation study. For this reason, we designed a mechanical robot frame that can mimic the bending motion of the knee joint, as shown

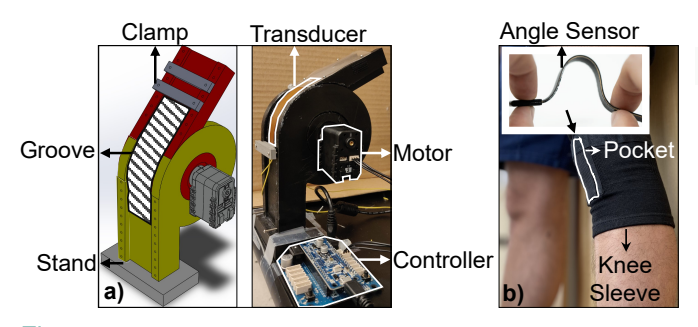


Fig. 3: a) The 3D printed robot frame to mimic the knee bending motion. b) The flexible angle measurement sensor and the knee sleeve to collect knee bending angle during gait.

in Figure 3(a). To use as input for the robot, we recorded the knee angle at six gait speeds, ranging from 2 mph to 7 mph with 1 mph increments. To obtain these recordings, we used a *BendLabs* flexible angle measurement sensor [44] placed inside the pocket on a knee sleeve worn by a subject, as shown in Figure 3(b). As an example, Figure 4(1a-1c) presents the data for three of these recordings. Thus, these recordings enabled the robot frame to mimic the knee bending motion as shown in Figure 5(a). Section V-A describes the robot frame and its actuation in more detail for readers interested in reproducing our results.

To harvest the motion energy, we place the MFC8528P2 flexible piezoelectric transducers [45] on the robot frame. Figure 5 summarizes the steps in our experimental evaluation. In Section IV-B, to measure the generated power, we first connect the transducers to a variable resistance box and record the voltage on the resistor, as illustrated in Figure 4(2a-2c). This section also presents the modeling results. Then, we connect the transducers to an energy harvester built around the LTC3331 power-management IC, developed by Linear Technology [46]. Section IV-C presents our measurement results regarding the amount of harvested energy after voltage rectification. Finally, Section IV-D presents the amount of energy delivered to a resistive load after losses due to voltage rectification and regulation. Figure 5(c) shows the specific measurement points within the LTC3331-based energy harvester used for the steps briefly described above for Section IV-C and Section IV-D.

# B. Generated Power by Piezoelectric Transducers

This section presents the power generated by the piezoelectric transducer when it is terminated by pure resistance (i.e., when the LTC3331-based energy harvester is not connected). To this end, we connect the terminals of the piezoelectric transducer to a variable resistor, and sweep the load resistance  $R_L$  from  $50\mathrm{k}\Omega$  to  $1.5\mathrm{M}\Omega$ . We connect a 1  $\Omega$  current-sensing resistor in series to  $R_L$ , and record the voltage on this sensing resistance at 1 kS/s for 25 seconds with an NI DAQ (Digital Acquisition) system. We discard the data from the first 5

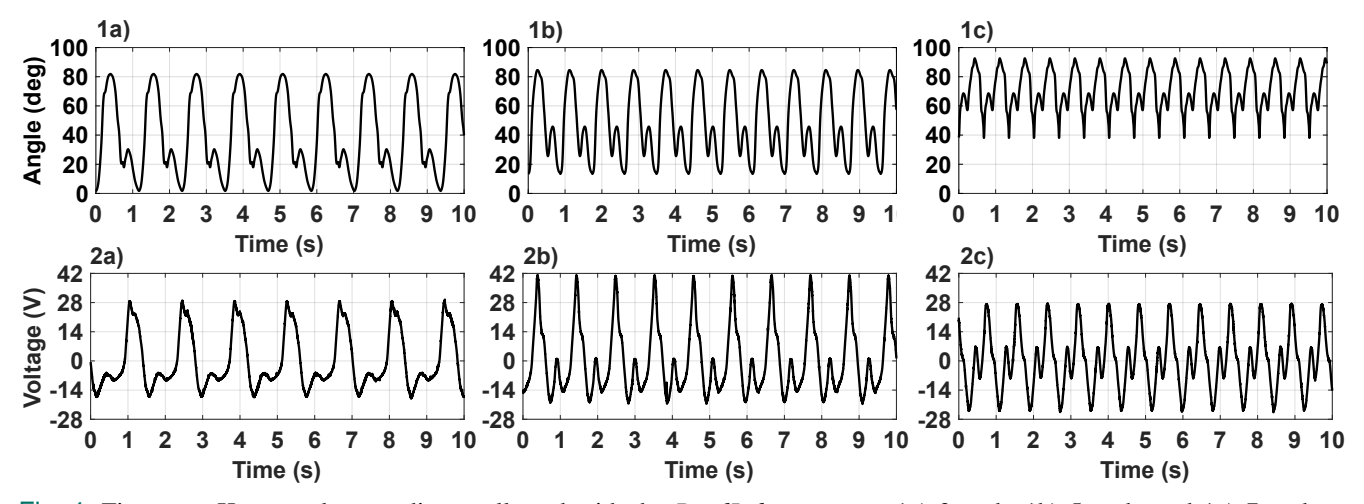


Fig. 4: First row: Knee angle recordings collected with the *BendLabs* sensor at 1a) 3 mph, 1b) 5 mph, and 1c) 7 mph. Second row: The corresponding voltage recordings from parallel MFC8528P2s at 2a) 3 mph, 2b) 5 mph, and 2c) 7 mph.

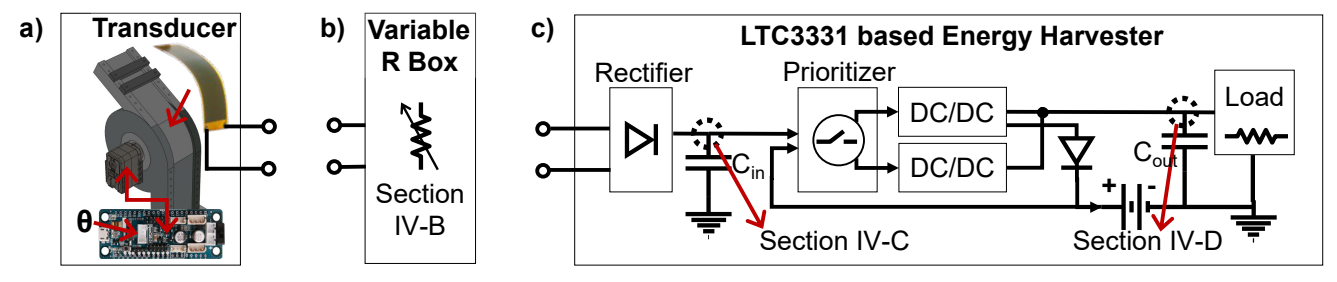


Fig. 5: Overview of our experimental evaluation a) input actuation and transducer placement, b) the measurement point in Section IV-B, c) the measurement points in Sections IV-C and IV-D

seconds, and obtain the RMS current  $I_{RMS}$  delivered to the load resistor from the remaining 20-second recording. Then, we simply calculate the RMS power  $P_{RMS}$  by using the following expression:  $P_{RMS} = I_{RMS}^2 R_L$ .

To analyze the effect of connection topology on generated power, we experiment with two configurations: (1) two bonded MFC8528P2 transducers connected in *series*, and (2) two bonded MFC8528P2 transducers connected in parallel. The transducers are bonded into a bimorph with an epoxy layer in the middle. The layer thicknesses and values for other experimental parameters are given in Table IV. For the series configuration, we connect the (+) terminal of the first unimorph to the (-) terminal of the second unimorph, and expose the (-) terminal of the first unimorph and (+) terminal of the second unimorph as the output terminals. For the parallel configuration, we connect the (-) terminals of both unimorphs to each other, and expose it as the negative output. Similarly, we do the same for the (+) terminals and expose it as the positive output. This way, we guarantee that the voltages do not add up destructively.

For each gait speed, we obtain the modeling results from Equation 16. The value of the fitting parameter f for each case is given in the Appendix. In what follows, we illustrate the results for the 3 mph, 5 mph, and 7 mph gait speeds, which correspond to walking, jogging and running for an average person. However, we emphasize that the reported results for modeling accuracy are from all gait speeds. The Mean Absolute Percentage Error (MAPE) for each case is given in the Appendix.

**Series Topology:** Figure 6(a) shows the P-V curves for three gait speeds when *two bonded transducers in series* serve as the transducer. The analytical results and the experimental measurements are in close agreement with each other. Specifically, the MAPE over all gait speeds (2–7 mph) is 2.1%.

One particular observation from the above results is that the MPP of the 5 mph curve is higher than that of the 7 mph curve, as depicted in Figure 6(b). Specifically, the maximum

TABLE IV: Parameter values used in our experiments.

Symbol	Value	Symbol	Value
L, W (mm)	85, 28	Yp (Gpa)	30.336
$h_p$ (µm)	180	C(nF)	$264\pm20\%$
$h_e^{\prime}$ (µm)	18	d31 (pC/N)	-170
$h_k$ (µm)	40	K, M	100
$h_{pc}$ (µm)	148	$R_L(\Omega)$	50k-1.5M
s0 (cm)	1.3	r (cm)	4

harvested power is close to 250  $\mu$ W at 5 mph, while it is close to 150  $\mu$ W at 7 mph. We can understand the root cause of this behavior by analyzing the knee angle waveforms in Figure 4(1a-1c). The range of the 5 mph waveform (15°–85°) is wider than the range of the 7 mph waveform (40°–90°). In addition, the 5 mph waveform has a shorter period than the 3 mph waveform. In other words, the former waveform repeats itself faster than the latter. These two effects, when combined, give rise to the sweet spot presented in Figure 6(b).

**Parallel Topology:** Figure 7(a) shows the P-V curves for three gait speeds when *two bonded transducers in parallel* serve as the transducer. The model results and the experimental measurements in this case are again in close agreement. Specifically, the average MAPE over all gait speeds is 3.2%, and again similar to the previous case, the maximum power point of the 5 mph curve is higher than that of the 3 and 7 mph curves as shown in Figure 7(b).

With the parallel configuration, the peak power for all gait speeds is greater than or equal to the corresponding power with the series configuration. However, the peaks in this case are at lower voltage levels than in the series configuration. For example, the maximum power point of the 5 mph curve is at 5.5 V in the parallel configuration, whereas it is at 9 V in the series configuration. The efficiency of the buck converter is

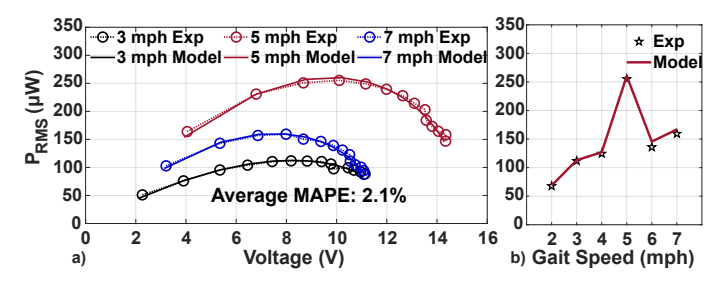


Fig. 6: Bonded piezoelectric transducers in series. a)  $P_{RMS}$  vs. voltage. b)  $P_{RMS}$  vs. gait speed.

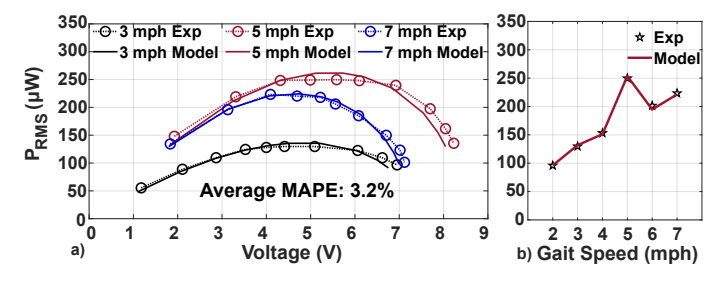


Fig. 7: Bonded piezoelectric transducers in parallel. a)  $P_{RMS}$  vs. voltage. b)  $P_{RMS}$  vs. gait speed.

higher at low input voltages than at high input voltages [46]. Thus, we use the parallel configuration in the rest of the experimental evaluations.

# C. Harvested Energy on Cin

In this section, we discuss the energy harvested at the input side of the LTC3331-based energy harvester, as shown in Figure 5(c). To this end, we utilize the full-wave bridge rectifier inside the LTC3331, which has an approximately 800-mV drop, and we connect a high-dielectric 22- $\mu$ F capacitor to the output of the rectifier (i.e., pin  $V_{IN}$  of LTC3331). Then, we measure the voltage waveform on the capacitor at several gait speeds, as shown in Figure 8. The details of LTC3331 operation principles are presented in Section V-C for the interested reader.

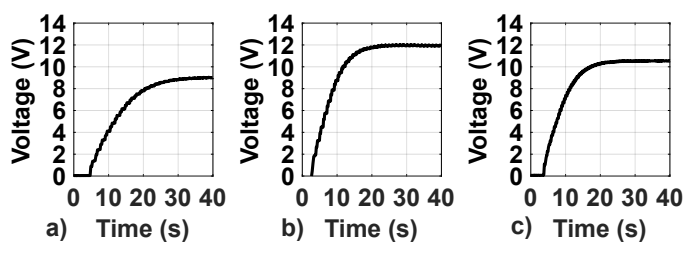


Fig. 8: Voltage on C<sub>in</sub> for a) 3 mph, b) 5 mph, and c) 7 mph

Operating at the Maximum Power Point: The harvester needs a suitable under voltage-lockout (UVLO) configuration to ideally operate at the maximum power point. Previous studies in the literature suggest setting the UVLO configuration to half of the rectified voltage level on the input capacitor so that the harvester can operate at the maximum power point [47]. Accordingly, the voltage levels in Figure 8 suggest that for the 3 mph condition, the optimal UVLO window configuration is 4-5 V. Similarly, for the 5 mph and 7 mph conditions, the optimal configuration is 5–6 V. To verify these settings empirically, we sweep the UVLO window configurations, as summarized in Table V. For each configuration, we record the energy on the input capacitor, as shown in Figure 9. The behavior in this figure is stemming from the UVLO configuration of the LTC3331. In this particular case, the peaks correspond to 6V (converted to energy using  $\frac{1}{2}CV^2$ ) and the dips correspond to 5V. The difference between a dip and a peak is the  $\Delta E_i$ , and  $\frac{\Delta E_i}{\Delta t_i}$  gives the average power for the  $i^{th}$ cycle. We average the power in several of these cycles from a 30-second recording to obtain an empirical average power figure  $P_{ava}$ , as presented in Table V. According to the results summarized in Table V, the UVLO window configurations that correspond to the maximum power point are consistent with the theory. Therefore, in the rest of our evaluations, we use 4-5 V for the 3 mph condition, and 5-6 V for the 5 mph and 7 mph conditions.

The harvested power obtained at 5 mph (161  $\mu$ W) is approximately 35% smaller than the power measurement shown in Figure 7. Similarly, the values obtained for the 3 mph and 7 mph conditions are considerably smaller than the corresponding power measurements in Figure 7. There

TABLE V:  $P_{avg}$  with various UVLO window configurations. **Bold** typeface shows the maximum value for each row.

	UVLO Configuration					
	3-4 V	4-5 V	5-6 V	6-7 V	7-8 V	9-10 V
3 mph 5 mph 7 mph	39 μW 100 μW 88 μW	<b>46</b> μ <b>W</b> 123 μ <b>W</b> 84 μ <b>W</b>	39 μW 161 μW 115 μW	33 μW 142 μW 94 μW	– 151 μW 94 μW	_ 132 μW _

are three main reasons for this difference: (1) The losses due to the integrated bridge rectifier, (2) the 22- $\mu$ F high-dielectric capacitor possessing approximately 20% capacitance degradation at 5 V, and (3) the purely resistive nature of the load in Figure 7 versus the capacitive nature of the input impedance of the rectifier. When combined with capacitor leakage current, these three factors lead to the relatively low power values obtained by the LTC3331-based energy harvester in this section.

# D. Harvested Energy on Cout

This section discusses the capacity of the energy harvester to power various load levels, as shown in Figure 5(c). We use the 5 mph condition as the input actuation and set the UVLO window to 5-6 V as noted in Table V. We configure the LTC3331 to regulate the output voltage at 1.8 V with three capacitance values: 150 μF, 620 μF, and 1150 μF. The load is a variable resistor that we sweep from 25 k $\Omega$  to 400 k $\Omega$ . For each load value, the output voltage is recorded for 20 seconds. From these recordings, we calculate the average output voltage and the percent ripple around these average values, as summarized in Figure 10. At high load-resistance values, the current drawn by the load is small and the output is easily regulated. At lower load-resistance values, the current and the ripple in the output voltage increase. For example, the output voltage cannot be regulated at 1.8 V with the 150-µF configuration if the load draws more than 10 µA. Specifically, the output voltage goes below 1.75 V, and the percent ripple exceeds 5%.

Increasing the capacitance has two main effects on the output voltage. First, it increases the load's turn-on time (i.e., the time it takes until regulation). At 150  $\mu$ F, the output voltage is regulated in 8.84 s, whereas at 1150  $\mu$ F, this time increases to 40.56 s. Second, the ripple in the output voltage decreases with higher capacitance. For an average load current of 35  $\mu$ A, the 150- $\mu$ F configuration has a 300-mV ripple amplitude. In comparison, the 1150- $\mu$ F configuration obtains 41 mV for

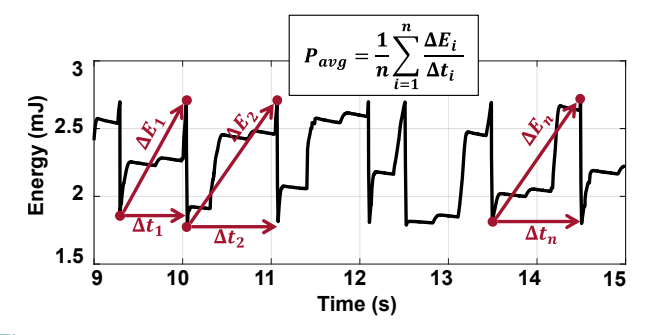


Fig. 9: The energy stored on  $C_{in}$  when UVLO window is set to 5–6 V at 5 mph gait speed.

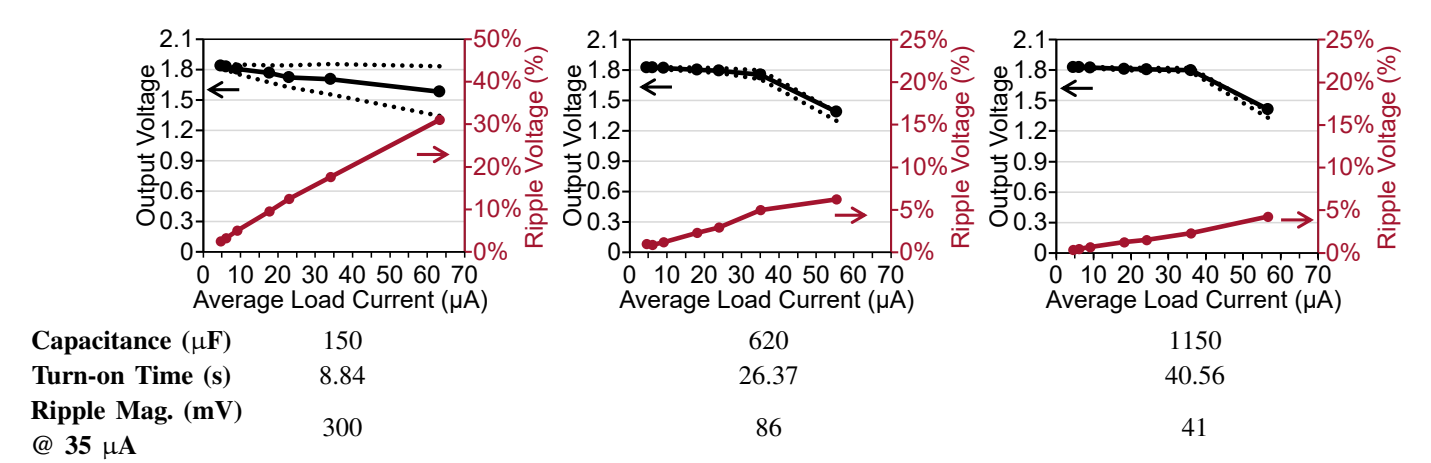


Fig. 10: Output voltage and ripple magnitudes for several output capacitance configurations.

the same load current. Therefore, designers should choose the output capacitance values depending on the application. For instance, if the load is not too sensitive to voltage ripples and has a broad input voltage range (e.g., 1.6~V-1.8~V), the  $150\mbox{-}\mu\text{F}$  configuration can sustain up to  $35\mbox{-}\mu\text{A}$  load current at 1.7~V with an approximately 20% ripple and an  $8.84\mbox{-}s$  turn-on time. If the load is sensitive, the  $620\mbox{-}\mu\text{F}$  configuration offers a tenfold reduction in ripple voltages at the expense of a three-fold increase in turn-on times.

## V. DISCUSSIONS ON THE EXPERIMENTAL PROCEDURE

This section describes the details of the experimental procedure to enable reproducibility of the results. In addition, we present valuable insights into the use of multiple piezoelectric transducers.

## A. Design, Fabrication & Actuation of the Knee Frame

The mechanical knee joint frame in Figure 3(a) is designed in SolidWorks. It is 3D printed using ABS plastic with 60% density for rapid prototyping. The design for the frame consists of three parts: the upper leg, kneecap, and lower leg. The kneecap has a 4-cm radius of curvature and is hollow in the middle. The upper leg is composed of an axle and the leg part. The axle is placed inside the hollow space in the kneecap. The bottom part of the kneecap is screwed to the top part of the lower leg, and the bottom part of the lower leg is screwed to a flat base to keep the frame upright. There is a 4-cm wide groove along all three sections in which the piezoelectric transducer is placed. The groove on the upper leg is covered for guided movement of the piezoelectric transducer to ensure good coupling to the bending motion. Also, several screw holes are placed along with the frame for mounting clampers to fix the piezoelectric transducer. Finally, the frame is actuated through a Dynamixel AX-12A servo motor 0.29° resolution, which is screwed to the outer side of the kneecap while the horn is screwed to the axle of the upper leg. The motor is controlled through a dedicated OpenCM9.04 control board.

To actuate the robot frame, we collect knee angle waveforms using a one-axis Bendlabs flexible angle sensor [44]. This sensor measures the angle between the tangent lines drawn from its two ends. Therefore, we place the sensor on the

knee using a compression sleeve, such that one end is on the thigh and the other end is on the shin. Using this setup, we capture the knee bending angle at various speeds on a treadmill for 125 seconds and discard the first 20 and last 5 seconds. With the remaining 100-second data, we generate ten 10-second segments and average them. Figure 4(1a-1c) shows the averaged segments for 3, 5, and 7 mph gait speed. Then, the averaged segment is fed to the motor controller to actuate the robot frame. This way, our robot frame mimics knee bending motion at various gait speeds, ranging from walking (2 mph) to running (7 mph).

#### B. Piezoelectric Transducers and Their Placement

PEHs use piezoelectric transducers to convert mechanical energy into electrical energy. In the current study, we use MFC8528P2 flexible piezoelectric transducers [45]. These transducers nicely fit inside the groove on our robot frame. We clamp the piezoelectric transducer from its wire-end to the lower leg. The other end of the piezoelectric transducer slides freely inside the groove in the knee frame to prevent any additional strain caused by unwanted stretching (i.e., the transducer is not clamped from the top).

Stacking multiple transducers is a promising solution to increase the generated current. Stacking does not result in any undue space overhead and poses no problems as long as the stacked transducers do not cause discomfort to the user. There are two ways to stack multiple transducers: (1) Stacking them on top of each other and fixing them from only one side, and (2) bonding two transducers with an epoxy layer in between them (e.g. a bimorph). The latter approach generates a higher current as a result of the higher strain in the piezoelectric layer due to the increased distance to the neutral axis. Our experience with the bonded structure shows that it does not cause any difficulties to the user during the knee bending motion.

The output of multiple piezoelectric transducers can be combined mainly by two different topologies. One option is to rectify and regulate the voltage produced by each transducer separately and then add the resulting DC voltages up. This approach incurs extra losses and design effort because each additional transducer requires its own rectifier and regulator. The other approach is to superimpose the harvested voltage

from all transducers and then to rectify and regulate the superimposed voltage. This approach may diminish the obtained power if the superimposed voltages add up destructively owing to synchronization issues. In our case, however, the bonded structure guarantees that no synchronization issues are present. Therefore, in this study, we superimpose the AC voltages generated by the piezoelectric transducers and rectify and regulate the superimposed voltage using the LTC3331 based energy harvester.

## C. LTC3331 Operation Principles

LTC3331 consists of a low-loss full-wave bridge rectifier and two buck DC/DC converters. The first DC/DC is connected to the input capacitor, while the other is connected to the battery, as illustrated in Figure 5(c). A prioritizer module with a programmable UVLO hysteresis window controls the operation of the DC/DC converters according to the voltage on the input and output capacitors. The charge generated by the piezoelectric transducer is rectified and stored on the input capacitance  $C_{in}$  connected to the  $V_{IN}$  pin of LTC3331. Once the voltage on  $C_{in}$  reaches the upper threshold of the UVLO window, the accumulated charge is transferred to the output capacitance through the first DC/DC. When the voltage on  $C_{in}$ decreases below the lower threshold of the UVLO window, the DC/DC is disabled. For example, the smallest window configuration turns on the first DC/DC when the voltage on  $C_{in}$  reaches 4 V and turns it off when the voltage goes down to 3 V. Then, the harvested energy starts accumulating again on the input capacitance. This process repeats until a regulated voltage at the output is obtained. If the voltage on the output capacitor can not be regulated, the second DC/DC is turned on to regulate the load using the battery. Thus, the UVLO configuration keeps the voltage on the input capacitor between the two values (as long as the load is regulated). For this reason, we choose the window configuration such that this voltage interval corresponds to the maximum power points presented in Figure 7.

## D. Effect of Temperature Variation on Energy Harvesting

We performed all of our experiments at standard room temperature. However, the temperature may vary depending on the time of year and the location in real-life use cases. Therefore, this section discusses the effect of temperature variation on the performance of MFC transducers.

The operating temperature for the MFC transducers is between -35°C and 85°C [45]. Marek et al. [48] analyzed the effect of temperature changes on the efficiency of MFC-based energy harvesters. They swept the operating temperature from -30°C to 70°C with 10°C steps. Their results revealed that the generated current by the MFC transducer decreases with increasing temperature. Specifically, the peak voltage at -30°C is twice the peak voltage at 70°C. They attributed this decrease to the change in the dielectric constant of the piezoelectric material from which the transducer's fibers were made.

The temperature range of interest for our wearable use case is between -20 $^{\circ}$ C and 40 $^{\circ}$ C. The results in [48] show a 1.4× decrease from -20 $^{\circ}$ C to 20 $^{\circ}$ C, and a 1.25× reduction from

 $20^{\circ}\text{C}$  to  $40^{\circ}\text{C}$ . Therefore, we expect the worst-case harvested energy (at  $40^{\circ}\text{C}$ ) to be 80% of the results presented in this work. Similarly, in the best case (at  $-20^{\circ}\text{C}$ ), it will be  $1.40\times$  larger than the presented results.

## VI. CONCLUSIONS & LIMITATIONS

Novel flexible and stretchable wearable devices require energy sources that match their physical properties. These physical constraints severely limit the use and the capacity of batteries. In this study, we argue that wearable energy harvesters, as orthogonal sources to batteries, can help satisfy the energy needs of wearable devices. However, the EH potential of wearable harvesters remains mostly unknown despite their promising potential. In this regard, we propose an analytical model of the EH potential of a wearable PEH placed on a knee joint. In addition, we provide extensive experimental validation of the proposed model with a prototype PEH. Our results show that the proposed model estimates the harvested power with less than 5% MAPE for all gait speeds and transducer configurations. In addition, the proposed harvester can obtain 161 µW at 5 mph, which can sustain a 35 µA constant load at 1.8V.

The power measurements in this study are performed at the maximum power point as we set the hysteresis windows based on the input actuation. However, in practice, operation at the maximum power point relies on distinct tracking algorithms [49]. Therefore, the accuracy of the tracking algorithm plays an important role on the amount of harvested power. In addition, in this study, we consider motion EH from the bending motion only. In actual use cases, other acting forces such as friction and the twisting and pulling of materials could increase the amount of energy harvested. Moreover, it is worth noting that the stiffness of the bonded structure can be noticeable for other joints (e.g., wrist, elbow, fingers), unlike the knee joint. Hence, studies focusing on the user experience present an important future research direction. Our current system prototype is constrained to desktop measurements as the many wires needed to connect different devices severely limit the portability of the system. As part of our future work, we plan to integrate the LTC3331 and the IoT device on the same printed circuit board (PCB). This integrated design will improve the portability of the system and enable taking measurements from a real subject performing different activities. Finally, to promote and facilitate future research in this field, we will open-source our datasets and models through our official gitlab repository<sup>1</sup>. More diverse EH data can help the research community accurately characterize the wearable EH potential for a vast range of use-cases.

https://git.doit.wisc.edu/engr/ece/elab/wearable-peh

#### **APPENDIX**

TABLE VI: Detailed values for mean absolute percentage error and fitting parameter f.

	Paralle			Series	<u> </u>
Speed	f	MAPE	Speed	f	MAPE
2 mph	0.12	3.4	2 mph	0.23	3.1
3 mph	0.13	4.16	3 mph	0.31	2.06
4 mph	0.14	3.11	4 mph	0.32	3.79
5 mph	0.21	4.16	5 mph	0.63	1.57
6 mph	0.35	2.44	6 mph	0.58	0.89
7 mph	0.49	1.99	7 mph	0.94	1.41
AVG 1	MAPE:	3.21	AVG M	IAPE:	2.14

#### REFERENCES

- Y. Tuncel, S. Bandyopadhyay, S. V. Kulshrestha, A. Mendez, and U. Y. Ogras, "Towards wearable piezoelectric energy harvesting: Modeling and experimental validation," in *Proceedings of the ACM/IEEE International Symposium on Low Power Electronics and Design*, 2020, pp. 55–60.
- [2] A. J. Espay et al., "Technology in Parkinson's Disease: Challenges and Opportunities," Mov Disord, vol. 31, no. 9, pp. 1272–1282, 2016.
- [3] J.-F. Daneault, "Could Wearable and Mobile Technology Improve the Management of Essential Tremor?" Frontiers in Neurology, vol. 9, pp. 257:1–257:8, 2018.
- [4] A. Tricoli, N. Nasiri, and S. De, "Wearable and Miniaturized Sensor Technologies for Personalized and Preventive Medicine," Advanced Functional Materials, vol. 27, no. 15, p. 1605271, 2017.
- [5] Y. Khan et al., "Flexible Hybrid Electronics: Direct Interfacing of Soft and Hard Electronics for Wearable Health Monitoring," Adv. Funct. Mater., vol. 26, no. 47, pp. 8764–8775, 2016.
- [6] M. Bariya, H. Y. Y. Nyein, and A. Javey, "Wearable sweat sensors," Nature Electronics, vol. 1, no. 3, pp. 160–171, 2018.
- [7] H. Jeong et al., "Modular and reconfigurable wireless e-tattoos for personalized sensing," Adv. Mater. Technol., vol. 4, no. 8, p. 1900117, 2019.
- [8] G. Bhat, R. Deb, and U. Y. Ogras, "Openhealth: open-source platform for wearable health monitoring," *IEEE Design & Test*, vol. 36, no. 5, pp. 27–34, 2019.
- [9] K. Sel, D. Osman, and R. Jafari, "Non-invasive cardiac and respiratory activity assessment from various human body locations using bioimpedance," *IEEE Open Journal of Engineering in Medicine and Biology*, 2021.
- [10] S. An, Y. Tuncel, T. Basaklar, G. K. Krishnakumar, G. Bhat, and U. Y. Ogras, "Mgait: Model-based gait analysis using wearable bend and inertial sensors," ACM Transactions on Internet of Things, vol. 3, no. 1, pp. 1–24, 2021.
- [11] A. Ozanne et al., "Wearables in Epilepsy and Parkinson's disease-A Focus Group Study," Acta Neurologica Scandinavica, vol. 137, no. 2, pp. 188–194, 2018.
- [12] DEKRA Testing and Certification, "FCCID Test Report USA FCC Part 15.247, 15.209." [Online] https://fccid.io/2AD7V-OURA2101/ Test-Report/67469RRF-002-5536194.
- [13] Oura Ring, "OURA The most accurate guide on Sleep, Readiness, and Activity." [Online] https://ouraring.com/, accessed 1 February 2022.
- [14] P. D. Mitcheson, E. M. Yeatman, G. K. Rao, A. S. Holmes, and T. C. Green, "Energy harvesting from human and machine motion for wireless electronic devices," *Proceedings of the IEEE*, vol. 96, no. 9, pp. 1457–1486, 2008.
- [15] S. Sudevalayam and P. Kulkarni, "Energy harvesting sensor nodes: Survey and implications," *IEEE Commun. Surv*, vol. 13, no. 3, pp. 443–461, 2010.
- [16] P. Jokic and M. Magno, "Powering smart wearable systems with flexible solar energy harvesting," in *IEEE International symposium on circuits* and systems (ISCAS), 2017, pp. 1–4.
- [17] S. Nguyen and R. Amirtharajah, "A hybrid rf and vibration energy harvester for wearable devices," in *IEEE Applied Power Electronics Conference and Exposition (APEC)*, 2018, pp. 1060–1064.

- [18] T. N. Huu, T. N. Van, and O. Takahito, "Flexible thermoelectric power generator with y-type structure using electrochemical deposition process," *Applied energy*, vol. 210, pp. 467–476, 2018.
- [19] Y. Tuncel, T. Basaklar, and U. Ogras, "How much energy can we harvest daily for wearable applications?" in *IEEE/ACM International* Symposium on Low Power Electronics and Design (ISLPED), 2021, pp. 1–6
- [20] P. Zeng, H. Chen, Z. Yang, and A. Khaligh, "Unconventional wearable energy harvesting from human horizontal foot motion," in *IEEE Applied Power Electronics Conference and Exposition (APEC)*, 2011, pp. 258– 264
- [21] K. Ylli, D. Hoffmann, A. Willmann, P. Becker, B. Folkmer, and Y. Manoli, "Energy harvesting from human motion: exploiting swing and shock excitations," *Smart Materials and Structures*, vol. 24, no. 2, p. 025029, 2015.
- [22] Q. Li, V. Naing, and J. M. Donelan, "Development of a biomechanical energy harvester," *Journal of neuroengineering and rehabilitation*, vol. 6, no. 1, pp. 1–12, 2009.
- [23] M. Pozzi and M. Zhu, "Plucked piezoelectric bimorphs for kneejoint energy harvesting: modelling and experimental validation," Smart Materials and Structures, vol. 20, no. 5, p. 055007, 2011.
- [24] C. Chen, L. Chen, Z. Wu, H. Guo, W. Yu, Z. Du, and Z. L. Wang, "3d double-faced interlock fabric triboelectric nanogenerator for bio-motion energy harvesting and as self-powered stretching and 3d tactile sensors," *Materials Today*, vol. 32, pp. 84–93, 2020.
- [25] Y. Zou, V. Raveendran, and J. Chen, "Wearable triboelectric nanogenerators for biomechanical energy harvesting," *Nano Energy*, vol. 77, p. 105303, 2020.
- [26] A. Proto, M. Penhaker, D. Bibbo, D. Vala, S. Conforto, and M. Schmid, "Measurements of generated energy/electrical quantities from locomotion activities using piezoelectric wearable sensors for body motion energy harvesting," Sensors, vol. 16, no. 4, p. 524, 2016.
- [27] G. Bassani, A. Filippeschi, and E. Ruffaldi, "Nonresonant kinetic energy harvesting using macrofiber composite patch," *IEEE Sens. J.*, vol. 18, no. 5, pp. 2068–2076, 2018.
- [28] A. Kansal, J. Hsu, S. Zahedi, and M. B. Srivastava, "Power management in energy harvesting sensor networks," ACM Trans. Embedd. Comput. Syst., vol. 6, no. 4, pp. 32–es, 2007.
- [29] Y. Tuncel, G. Bhat, J. Park, and U. Ogras, "Eco: Enabling energy-neutral iot devices through runtime allocation of harvested energy," *IEEE Internet of Things Journal*, pp. 1–1, 2021.
- [30] Y. Liu, H. Khanbareh, M. A. Halim, A. Feeney, X. Zhang, H. Heidari, and R. Ghannam, "Piezoelectric energy harvesting for self-powered wearable upper limb applications," *Nano Select*, 2021.
- [31] C. N. Teague, J. A. Heller, B. N. Nevius, A. M. Carek, S. Mabrouk, F. Garcia-Vicente, O. T. Inan, and M. Etemadi, "A wearable, multimodal sensing system to monitor knee joint health," *IEEE Sensors Journal*, vol. 20, no. 18, pp. 10323–10334, 2020.
- [32] B. J. Stetter, S. Ringhof, F. C. Krafft, S. Sell, and T. Stein, "Estimation of knee joint forces in sport movements using wearable sensors and machine learning," *Sensors*, vol. 19, no. 17, p. 3690, 2019.
- [33] Y. Cha, "Energy harvesting using flexible piezoelectric materials from human walking motion: Theoretical analysis," *Journal of Intelligent Material Systems and Structures*, vol. 28, no. 20, pp. 3006–3015, 2017.
- [34] M. Beyaz, "Energy harvesting from knee motion using piezoelectric patch transducers," APJES, vol. 7, no. 2, pp. 255–260, 2019.
- [35] G. Bhat, Y. Tuncel, S. An, H. G. Lee, and U. Y. Ogras, "An ultralow energy human activity recognition accelerator for wearable health applications," ACM Transactions on Embedded Computing Systems (TECS), vol. 18, no. 5s, pp. 1–22, 2019.
- [36] J. Loh, J. Wen, and T. Gemmeke, "Low-cost dnn hardware accelerator for wearable, high-quality cardiac arrythmia detection," in *IEEE Inter*national Conference on Application-specific Systems, Architectures and Processors (ASAP), 2020, pp. 213–216.
- [37] Y. Kuang, Z. Yang, and M. Zhu, "Design and characterisation of a piezoelectric knee-joint energy harvester with frequency up-conversion through magnetic plucking," *Smart Materials and Structures*, vol. 25, no. 8, p. 085029, 2016.
- [38] H. Kulah and K. Najafi, "Energy scavenging from low-frequency vibrations by using frequency up-conversion for wireless sensor applications," *IEEE Sensors Journal*, vol. 8, no. 3, pp. 261–268, 2008.
- [39] H. Zhou, Y. Zhang, Y. Qiu, H. Wu, W. Qin, Y. Liao, Q. Yu, and H. Cheng, "Stretchable piezoelectric energy harvesters and self-powered sensors for wearable and implantable devices," *Biosensors and Bioelectronics*, p. 112569, 2020.

- [40] A. Erturk and D. J. Inman, "A Distributed Parameter Electromechanical Model for Cantilevered Piezoelectric Energy Harvesters," *Journal of Vibration and Acoustics*, vol. 130, no. 4, 2008.
- [41] Erturk, Alper and Inman, Daniel J., "An experimentally validated bimorph cantilever model for piezoelectric energy harvesting from base excitations," Smart Materials and Structures, vol. 18, no. 2, p. 025009, 2009.
- [42] J. Park, H. Joshi, H. G. Lee, S. Kiaei, and U. Y. Ogras, "Flexible PV-cell Modeling for Energy Harvesting in Wearable IoT Applications," ACM Trans. Embedd. Comput. Syst., vol. 16, no. 5s, pp. 156:1–156:20, 2017.
- [43] N. G. Elvin and A. A. Elvin, "Large deflection effects in flexible energy harvesters," *Journal of Intelligent Material Systems and Structures*, vol. 23, no. 13, pp. 1475–1484, 2012.
- [44] Bend Labs, "Flexible Single Axis Bidirectional Sensor," [Online] https://www.bendlabs.com/, accessed 1 February 2022.
- [45] Smart-Material, "MFC P2 and P3 types," https://www.smart-material. com/MFC-product-P2.html, accessed 1 February 2022.
- [46] Linear Technology, "LTC3331 Nanopower Buck-Boost DC/DC with Energy Harvesting Battery Charger," [Online] https://www.analog.com/ en/products/ltc3331.html/, accessed 1 February 2022.
- [47] G. K. Ottman, H. F. Hofmann, and G. A. Lesieutre, "Optimized piezoelectric energy harvesting circuit using step-down converter in discontinuous conduction mode," *IEEE Trans. Power Electron.*, vol. 18, no. 2, pp. 696–703, 2003.
- [48] M. Płaczek and G. Kokot, "Modelling and laboratory tests of the temperature influence on the efficiency of the energy harvesting system based on mfc piezoelectric transducers," *Sensors*, vol. 19, no. 7, p. 1558, 2019
- [49] S. Fang, H. Xia, Y. Xia, Y. Ye, G. Shi, X. Wang, and Z. Chen, "An efficient piezoelectric energy harvesting circuit with series-sshi rectifier and fnov-mppt control technique," *IEEE Transactions on Industrial Electronics*, vol. 68, no. 8, pp. 7146–7155, 2020.